Nanoscale

PAPER

View Article Online
View Journal | View Issue

Cite this: *Nanoscale*, 2019, **11**, 13282

Intermetallic SnSb nanodots embedded in carbon nanotubes reinforced nanofabric electrodes with high reversibility and rate capability for flexible Li-ion batteries†

Renpeng Chen,[a] Xiaolan Xue,[a] Yi Hu,[a] Weihua Kong,[a] Huinan Lin,[a] Tao Chen[a] and Zhong Jin *[a,b]

Received 31st May 2019,
Accepted 26th June 2019

DOI: 10.1039/c9nr04645c

rsc.li/nanoscale

Tin (Sn) based anode materials have been regarded as promising alternatives for graphite in lithium ion batteries (LIBs) due to their high theoretical specific capacity and conductivity. However, their practical application is severely restrained by the drastic volume variation during cycling processes. Here we report the preparation of intermetallic SnSb nanodots embedded in carbon nanotube reinforced N-doped carbon nanofibers (SnSb-CNTs@NCNFs) as a free-standing and flexible anode for LIBs. In this unique structure, the SnSb nanodots are well protected by the NCNFs and exhibit greatly reduced volume change. The mechanical strength and conductivity of the nanofabric electrode are further improved by the embedded CNTs. Benefiting from these advantages, the SnSb-CNTs@NCNFs anode delivers a high reversible capacity of 815 mA h g^{-1} at 100 mA g^{-1}, a high rate capability (370 mA h g^{-1} at 5000 mA g^{-1}) and a long cycle life (451 mA h g^{-1} after 1000 cycles at 2000 mA g^{-1}). When assembled into flexible pouch cells, the full cells based on SnSb-CNTs@NCNFs anodes also exhibit high flexibility and good lithium storage performances.

Introduction

Lithium-ion batteries (LIBs) have been considered as the most representative energy storage system for electric vehicles (EVs), portable electronic devices and smart grids, owing to their high energy density and operating voltage.[1–6] Although great progress has been achieved in the commercial graphite anode, low theoretical capacity (372 mA h g^{-1}) and poor rate performance make it difficult to meet the surging demands of the market.[7,8] Moreover, LIBs also suffer from the safety issues caused by the formation of lithium dendrites due to the low Li^+ insertion/extraction potentials of graphite.[9,10] In addition, the insulating polymer binder used in traditional LIBs also lowers the conductivity and energy density.[11–13] Therefore, it is essential to develop alternative anode materials with higher reversible capacity, better rate capability and longer cycling stability.

In recent years, group IV and V materials (Si,[14,15] Ge,[16] Sn,[17,18] P,[19,20] Sb[21,22] and Bi[23]) have attracted increasing attention as appealing alternatives for the graphite anode owing to their high theoretical capacity. Among them, Sn and Sb have some outstanding properties, such as good specific capacity (~1000 and 660 mA h g^{-1}, respectively), high volumetric energy density (~7300 and 1750 mA h cm^{-3}, respectively), good electrical conductivity, and safer operation potential (~0.4–0.9 V *vs.* Li/Li^+).[24,25] However, like Si-based anodes, Sn and Sb-based materials also suffer from dramatic capacity fading originating from the large volume variation and pulverization during repeated Li insertion/extraction processes.[26,27] Notably, it has been reported that the intermetallics composed of two or more metals may exhibit less volume variation due to the different redox potentials of the metals during lithiation/delithiation processes, which can greatly enhance the electrochemical performances (as shown in Table S1†).[28–38] Unfortunately, the specific capacities, cycle life and rate capability of SnSb-based anodes are not fully satisfactory. The main reason could be attributed to the large particle size of SnSb intermetallics, which is not conducive to the effective utilization of active materials, leading to the low specific capacity. On the other hand, the solid–electrolyte interface (SEI) film on the electrode surface may crack and reform repeatedly owing to the pulverization of active

[a]*Key Laboratory of Mesoscopic Chemistry of MOE, Jiangsu Key Laboratory of Advanced Organic Materials, School of Chemistry and Chemical Engineering, Nanjing University, Nanjing 210023, China. E-mail: zhongjin@nju.edu.cn*
[b]*Shenzhen Research Institute of Nanjing University, Shenzhen 518063, China*
†Electronic supplementary information (ESI) available. See DOI: 10.1039/c9nr04645c

materials, resulting in poor cycle life. Undoubtedly, it is very important to rationally design the compositions and microstructures of electrode materials for improving the Li-storage performances.

Ideally, high-performance anode materials based on intermetallics should have the following features: (1) the size of intermetallic nanocrystals should be in the sub-10 nm scale to provide high interfacial areas, ensuring the full use of active materials and mitigating the absolute volume expansion during cycling. (2) The intermetallic nanocrystals should be confined in other stable and conductive matrices to prevent the pulverization/agglomeration during the repeated cycling processes. (3) The use of insulating polymer binders should be avoided for assembling the cells to enhance the energy density and reaction kinetics.[39,40]

Following this line of thought, here we report a feasible strategy to fabricate well-dispersed intermetallic SnSb nanodots confined in the carbon nanotube reinforced nitrogen-doped carbon nanofibers (SnSb-CNTs@NCNFs) as a binder-free and current-collector-free anode with outstanding electrochemical performances and flexibility for LIBs. The highly conductive and stable matrix of intertwined CNTs@NCNFs can effectively prevent the agglomeration of SnSb nanodots, protect them from being corroded by the electrolyte, and accommodate the volume change during the repeated cycles. In addition, the CNTs embedded in the nanofabric electrode are capable of improving the flexibility and local conductivity, leading to enhanced rate performance. These characteristics endow the flexible and free-standing SnSb-CNTs@NCNFs electrodes with excellent lithium storage performances.

Experimental section

Materials synthesis

The SnSb-CNTs@NCNFs electrode was obtained by an electrospinning process followed by a high temperature annealing treatment. Typically, 0.2 g of polyacrylonitrile (PAN) was dissolved in 2.0 mL of *N*,*N*-dimethylformamide (DMF) by vigorous stirring at 80 °C for 1 h. Then, 0.6 mmol of tin(II) chloride dihydrate ($SnCl_2{\cdot}2H_2O$) and 0.6 mmol of antimony trichloride ($SbCl_3$) were added into the solution and stirred for 2 h. Subsequently, 10 mg of multi-walled CNTs (Xianfeng Nano Corp.) with the diameter range of 20–40 nm was added into the above clear solution. The solution was agitated intermittently and ultrasonicated for 8 h to obtain a homogeneous precursor solution. The precursor solution was added into a 5 mL plastic syringe equipped with a blunt tip needle (21-gauge), which was connected with a high voltage power supply. A piece of aluminum foil was used for collecting the nanofibers obtained by electrospinning. A syringe pump was used to control the solution feeding rate at 0.15 mL h^{-1}, and the distance between the blunt tip needle and the aluminum foil was set to be 15 cm. A high voltage of 20 kV was applied between the blunt tip needle and the aluminum foil to initiate electrospinning. After electrospinning for 10 h, the precursor mat was stripped off from the aluminum foil. To obtain the free-standing SnSb-CNTs@NCNFs, the as-prepared mat was stabilized at 250 °C for 5 h and then carbonized at 700 °C for 1 h under a high-purity N_2 atmosphere. The temperature ramp rates of the two heating steps were set to be 2 °C min^{-1} and 5 °C min^{-1}, respectively. As control samples, Sn-CNTs@NCNFs or Sb-CNTs@NCNFs were synthesized through the same processes except adding 1.2 mmol of $SnCl_2{\cdot}2H_2O$ or $SbCl_3$ into the PAN/DMF solution. The SnSb@NCNFs control sample was also prepared without the addition of CNTs.

Characterization studies

The morphology of the samples was characterized using a scanning electron microscope (SEM, Hitachi S-4800). The microstructure was studied on a JEM-2100 transmission electron microscope (TEM). The powder X-ray diffraction spectra (XRD) were recorded on an X-ray diffractometer (Bruker D-8 Advance, Cu Kα radiation source). The content of SnSb was measured through a thermo-gravimetric analysis (TGA, Netzsch STA 449 C) method from ambient temperature to 800 °C under air atmosphere with a heating rate of 5 °C min^{-1}. The X-ray photoelectron spectra (XPS) were obtained on a VersaProbe X-ray photoelectron spectrometer (PHI-5000, Al Kα radiation source). The Raman spectra were collected with a Horiba JY Raman spectrometer using a 473 nm laser source. Brunauer–Emmett–Teller (BET) analysis was used to collect the N_2 adsorption–desorption isotherms at 77 K on a Quantachrome Instruments. The specific surface areas were calculated using the BET method and the pore size distribution was obtained using the Barrett–Joyner–Halenda (BJH) method.

Electrochemical measurements

For half-cell tests, CR2032 coin cells were assembled in an Ar-filled glovebox with the oxygen and water contents below 0.1 ppm. The calcined nanofabrics were cut into self-standing electrodes with a diameter of 14 mm, which were directly assembled into the cells without mechanical milling or slurry coating steps. Neither additives (Ketjen black and polymer binder) nor a metal current collector was used for the nanofabric electrode. The areal density of the prepared electrodes was about 2.5 mg cm^{-2}. Lithium foil and Celgard 2400 membrane served as the counter electrode and the separator, respectively. The electrolyte is 1.0 M $LiPF_6$ solution in the co-solvent of dimethyl carbonate (DMC) and ethylene carbonate (EC) (1 : 1 by volume). Cyclic voltammetry (CV) and electrochemical impendence spectroscopy (EIS) were performed on a Chenhua CHI-760 electrochemical workstation. Galvanostatic charge/discharge tests were carried out between 0.01 and 3.0 V *vs.* Li/Li^+ at various current densities on a LAND battery-test instrument (CT2001A). All the applied current densities used in this study were based on the total mass of the SnSb-CNTs@NCNFs composites.

For the assembly of soft-packed full batteries, SnSb-CNTs@NCNFs, $LiFePO_4$ coated on aluminum foil and glass fiber (Whatman) served as the anode, cathode and

separator, respectively. For the preparation of the $LiFePO_4$ cathode, commercialized $LiFePO_4$ (MTI. Corp.), Ketjen black, and poly(vinylidene fluoride) (PDVF) were mixed in a weight ratio of 8 : 1 : 1 and dispersed in *N*-methyl-2pyrrolidinone (NMP) to form a homogeneous slurry. The slurry was then coated on aluminum foil and dried at 90 °C for 12 h under vacuum. Before being assembled, the SnSb-CNTs@NCNFs electrode was prelithiated by attaching together with lithium foil and immersing in the electrolyte for 5 h in the glovebox.

Results and discussion

The overall synthetic route to SnSb-CNTs@NCNFs is illustrated in Scheme 1a and also described in detail in the Experimental section. First of all, multi-walled CNTs were homogeneously dispersed into a polyacrylonitrile/*N*,*N*-dimethylformamide (PAN/DMF) solution containing $SnCl_2{\cdot}2H_2O$ and $SbCl_3$ (in a molar ratio of 1 : 1). The mixed precursor solution was electrospun into a flexible nonwoven nanofabric. Finally, the nanofabric was stabilized at 250 °C and completely carbonized at 700 °C to obtain SnSb-CNTs@NCNFs. During this thermal treatment process, the $SnCl_2{\cdot}2H_2O$ and $SbCl_3$ salts were converted to intermetallic SnSb nanodots homogeneously embedded in the CNTs reinforced NCNFs. Different from the conventional electrostatic spinning products, the addition of carbon nanotubes can further improve the conductivity and flexibility of the nanofabric electrodes at the same time, as shown in Scheme 1b. We also prepared Sn-CNTs@NCNFs, Sb-CNTs@NCNFs, and SnSb@NCNFs electrodes as control samples for comparing the electrochemical performances, as depicted in detail in the Experimental section.

The microstructure of the as-obtained SnSb-CNTs@NCNFs electrodes was investigated by scanning electron microscopy (SEM) and transition electron microscopy (TEM). As presented in Fig. 1a and b, the unannealed precursor fabrics display a homogeneous fibrillar structure with a smooth and clear surface, indicating that the carbon nanotubes, $SnCl_2{\cdot}2H_2O$ and $SbCl_3$ are encapsulated in the nanofibers. After stabilization and carbonization, the final product well preserved the uniform nanofibrous structure, exhibiting a diameter range of 300–400 nm (Fig. 1c and d). Fig. 1e and f display the TEM images of the as-prepared SnSb-CNTs@NCNFs composite under different magnifications, which clearly show the SnSb nanodots uniformly embedded in the NCNFs. Some CNTs are adhered to the surface of the NCNFs (Fig. 1e and f), making the surface rougher, in good agreement with the results of SEM images (Fig. 1c and d). As indicated by the red circles in Fig. 1b and f, the CNTs are connected and inserted into the interior of the nanofabrics, thus efficiently improving the electrical conductivity of electrodes. The high-resolution TEM (HRTEM) image (Fig. 1g) presents the SnSb nanodots encapsulated in NCNFs with the size around 2 nm and the ordered lattice fringes of 0.30 nm, corresponding to the (101) planes of SnSb. Energy-dispersive spectroscopy (EDX) elemental mappings (Fig. 2h and i) demonstrate the uniform distribution of C, N, Sn and Sb elements in SnSb-CNTs@NCNFs. Similarly, the survey X-ray photoelectron spectroscopy (XPS) analysis (Fig. S1†) also confirms the presence of C, N, Sn and Sb elements.

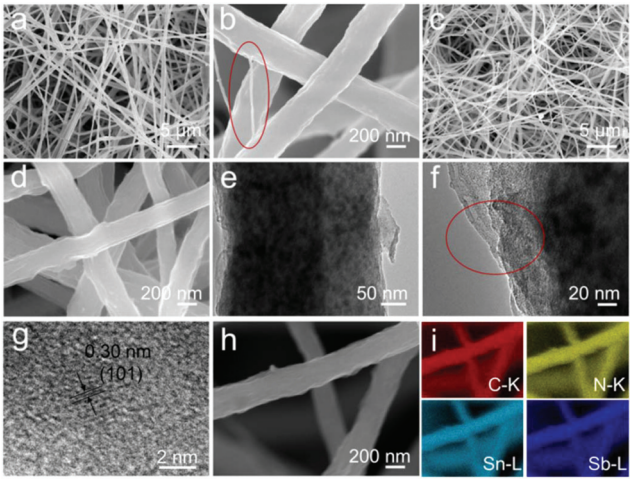

Fig. 1 Morphological and structural characterization studies of the as-prepared samples. (a, b) FESEM images at low and high magnifications of the unannealed precursor fabrics. (c, d) FESEM images of SnSb-CNTs@NCNFs. (e–g) TEM and HRTEM images of SnSb-CNTs@NCNFs. (h, i) FESEM image and the corresponding elemental mappings of SnSb-CNTs@NCNFs, respectively.

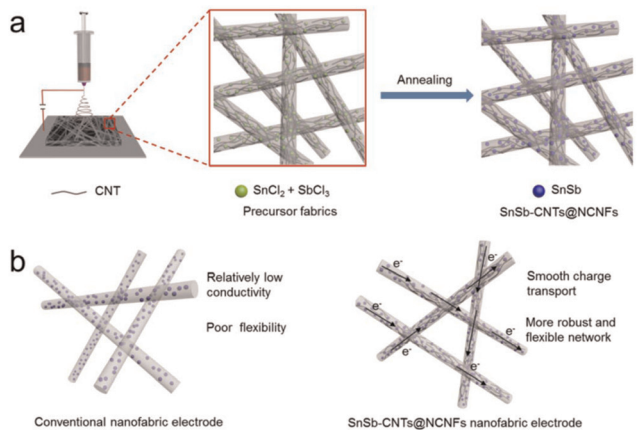

Scheme 1 (a) Schematic preparation method of SnSb-CNTs@NCNFs electrodes. (b) Schematic comparison of SnSb@NCNFs and SnSb-CNTs@NCNFs.

Fig. 2a shows the X-ray diffraction (XRD) pattern of SnSb-CNTs@NCNFs, and all distinct peaks can be well indexed to carbon or intermetallic SnSb alloy (hexagonal phase, JCPDS Card No. 33-0118). No obvious peaks of elemental Sn and Sb are observed, indicating that the nanodots embedded in the NCNFs are composed of SnSb. The Raman spectrum of SnSb-CNTs@NCNFs displays two broad peaks located at ~1368 and ~1577 cm^{-1}, corresponding to the D and G bands of carbon, respectively (Fig. 2b). The intensity ratio of D and G bands (I_D/I_G) is calculated to be 1.04, indicating a partially graphitic structure with large disorder. The C 1s XPS spectrum (Fig. 2c)

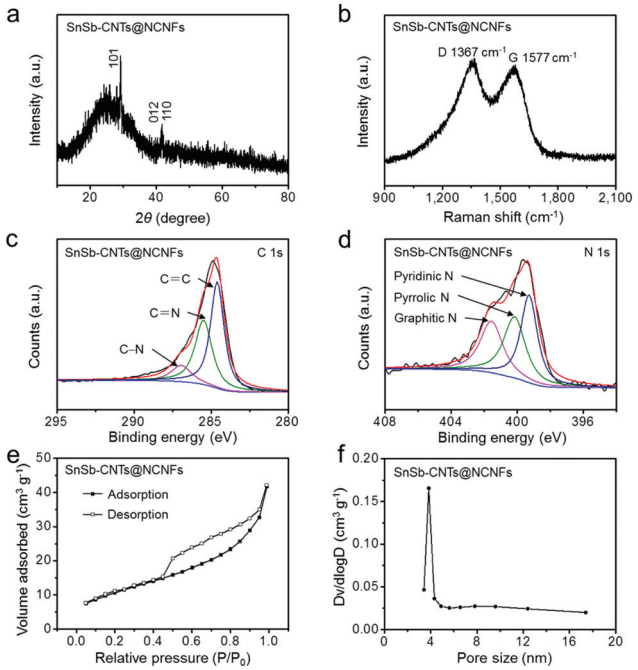

Fig. 2 Characterization studies of the as-obtained SnSb-CNTs@NCNFs. (a) XRD pattern and (b) Raman spectrum. (c, d) High-resolution XPS spectra in (c) C 1s and (d) N 1s regions. (e) Nitrogen adsorption–desorption isotherms and (f) pore size distribution.

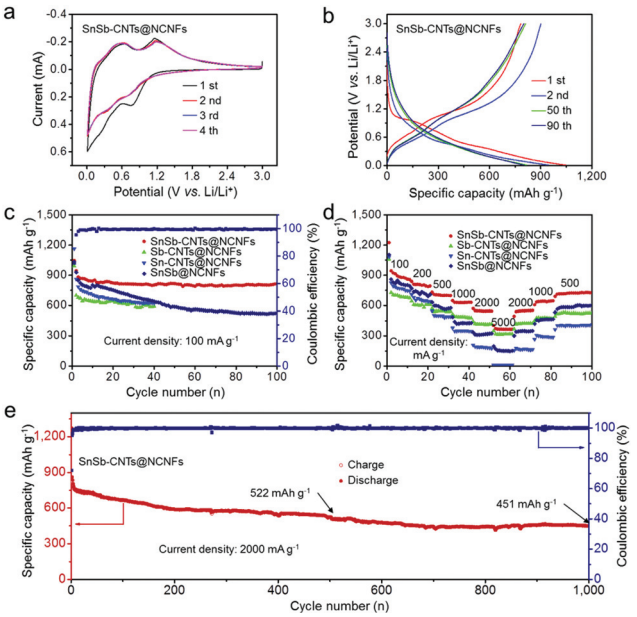

Fig. 3 Electrochemical characterization studies of the as-prepared samples as anode materials in LIBs. (a) CV profiles of the SnSb-CNTs@NCNFs electrode during the initial four cycles between 0.01 and 3 V *vs.* Li/Li^+ at a scan rate of 0.2 mV s^{-1}. (b) Discharge–charge curves of the SnSb-CNTs@NCNFs electrode at a current density of 100 mA g^{-1}. (c) Cycling performances and (d) rate capabilities of SnSb-CNTs@NCNFs, Sb-CNTs@NCNFs, Sn-CNTs@NCNFs and SnSb@NCNFs electrodes at different current densities, respectively. (e) Long-term cycling performance of the SnSb-CNTs@NCNFs electrode at a large current density of 2000 mA g^{-1}.

can be deconvoluted into three peaks located at 286.9 eV for C–N (11.4 at%), 285.5 eV for C═N (38.4 at%) and 284.6 eV for C═C (50.2 at%), respectively. Likewise, the N 1s XPS spectrum (Fig. 2d) presents three types of N forms in SnSb-CNTs@NCNFs, namely graphitic N (401.5 eV, 29.3 at%), pyrrolic N (400.2 eV, 33.9 at%) and pyridinic N (399.3 eV, 36.8 at%), respectively. N_2 adsorption–desorption isotherms were measured to investigate the specific surface area and pore structure of SnSb-CNTs@NCNFs (Fig. 2e and f). The specific surface area was calculated to be about 38.7 m^2 g^{-1}. The type-*IV* curve reveals the mesoporous structure of SnSb-CNTs@NCNFs with a narrow pore size distribution and an average pore size of 3.8 nm. In order to measure the mass content of SnSb in SnSb-CNTs@NCNFs, thermogravimetric analysis (TGA) under air atmosphere was performed and the XRD pattern of the solid residue after the TGA test was obtained, as presented in Fig. S2.† The small weight loss of ~4.8 wt% from room temperature to 200 °C is attributed to the removal of the absorbed water, while the weight loss of ~29.0 wt% between 200 and 800 °C is ascribed to the oxidation of carbon and SnSb (Fig. S2a†). The XRD peaks of the solid residue after the TGA test are well indexed to SnO_2 (JCPDS Card No. 41-1445) and Sb_2O_4 (JCPDS Card No. 11-0694) (Fig. S2b†). Therefore, the weight ratio of SnSb in the SnSb-CNTs@NCNFs can be calculated to be 54.9 wt%, indicating the relatively high loading mass of SnSb in the electrode.

The electrochemical performances of the as-prepared samples were characterized as anode materials by assembling into coin cells with lithium foils as counter electrodes (Fig. 3). Cyclic voltammograms (CV) were used to investigate the electrochemical properties of SnSb-CNTs@NCNFs during lithiation/delithiation processes (Fig. 3a). The obvious reduction peak at 1.04 V *vs.* Li/Li^+ is observed in the 1st cycle but disappeared in the following cycles, owing to the formation of the solid electrolyte interphase (SEI) layer caused by the reductive decomposition of the electrolyte. In the cathodic process, the peak at ~0.85 V is ascribed to the formation of Li_3Sb. The peaks from ~0.7 V to 0.3 V are assigned to the lithiation of Sn to yield various phases of Li_xSn ($0 \le x \le 4.4$). The reaction sequence is reversed in the anodic process. The peaks between 0.4 and 0.8 V located around 1.1 V correspond to the delithiation of Li_xSn and Li_3Sb, respectively. The general Li-storage reactions of SnSb-CNTs@NCNFs can be summarized according to the previous literature:[32–37]

$$SnSb + 3Li \leftrightarrow Li_3Sb + Sn \quad (1)$$

$$Li_3Sb + Sn + xLi \leftrightarrow Li_3Sb + Li_xSn \ (0 \le x \le 4.4). \quad (2)$$

Because the lithiation/delithiation potentials of Sn and Sb are different, only one element is lithiated/delithiated at a time, while the other serves as a buffer, leading to the much smooth volume change and good electrochemical performances of SnSb.[35,36] Notably, the CV curves after the 1st cycle have an excellent overlap, suggesting the high reversibility and good cycling capability of SnSb-CNTs@NCNFs. Fig. 3b displays the typical discharge–charge curves of the SnSb-CNTs@NCNFs elec-

trode at a current density of 100 mA g^{-1} between 0.01 and 3.0 V. The initial specific discharge and charge capacities are 1044 mA h g^{-1} and 783 mA h g^{-1}, respectively, corresponding to a high initial coulombic efficiency of 75.0%. The electrolyte decomposition and the inevitable formation of the SEI layer should account for the initial irreversible capacity loss. The discharge–charge curves in the 50th and 90th cycles are almost overlapped, indicating the good stability of the SnSb-CNTs@NCNFs electrode.

To make comparisons of the Li^+ storage properties among the SnSb-CNTs@NCNFs, Sb-CNTs@NCNFs, Sn-CNTs@NCNFs and SnSb@NCNFs electrodes, the cycling performances of these electrodes were tested at a current density of 100 mA g^{-1}. As depicted in Fig. 3c, the initial specific discharge capacities of SnSb-CNTs@NCNFs, Sb-CNTs@NCNFs, Sn-CNTs@NCNFs and SnSb@NCNFs are 1044, 991, 1164 and 1034 mA h g^{-1}, respectively. The reversible capacities of Sb-CNTs@NCNFs, Sn-CNTs@NCNFs and SnSb@NCNFs decrease from 700, 861 and 929 mA h g^{-1} (at the 2nd cycle) to 589, 622 and 639 mA h g^{-1} (at the 40th cycle), respectively. This could be explained by the fact that the Sb-CNTs@NCNFs, Sn-CNTs@NCNFs and SnSb@NCNFs anodes suffer from more serious pulverization during the discharge–charge processes, leading to a relatively rapid capacity fading. In contrast, the SnSb-CNTs@NCNFs electrode presents the best cycling performance, delivering a high reversible discharge capacity of 815 mA h g^{-1} after 100 cycles, which is around 86% of the discharge capacity in the 2nd cycle (945 mA h g^{-1}). What is more, the coulombic efficiency of the SnSb-CNTs@NCNFs electrode is also very outstanding, which rapidly increases from 75.0% at the 1st cycle to 99.4% at the 8th cycle, and remains above 99% in the later cycles, demonstrating the reversible Li^+ storage and smooth charge transport properties of the SnSb-CNTs@NCNFs electrode. The rate capabilities were also evaluated at different current densities (Fig. 3d). The SnSb-CNTs@NCNFs electrode delivers high reversible capacities of 914, 808, 706, 630, 550 and 370 mA h g^{-1} at the current densities of 100, 200, 500, 1000, 2000 and 5000 mA g^{-1}, respectively. When the current densities go back to 2000, 1000 and 500 mA g^{-1}, the discharge capacities restore to 544, 640 and 715 mA h g^{-1}, respectively, indicating the good rate performance. In contrast, the Sb-CNTs@NCNFs, Sn-CNTs@NCNFs and SnSb@NCNFs electrodes exhibit much lower rate capabilities, further confirming the structural superiority of SnSb-CNTs@NCNFs.

To further explain the reason for the superior performances of SnSb-CNTs@NCNFs, the microstructure of control samples (Sn-CNTs@NCNFs, Sb-CNTs@NCNFs and SnSb@NCNFs) was also characterized (Fig. S3†). As presented in Fig. S3a and d,† due to the low melting point of Sn (231.89 °C), metal Sn tends to form large spheres with a diameter of ~400 nm on the surface of NCNFs, which cannot be well encapsulated in the NCNFs, leading to the unstable electrochemical performances. Although the microstructure of Sb-CNTs@NCNFs (Fig. S3b and e†) is similar to that of SnSb-CNTs@NCNFs, and the Sb nanoparticles are well embedded in the Sb-CNTs@NCNFs, the electrochemical performance of Sb-CNTs@NCNFs is still inferior to that of SnSb-CNTs@NCNFs, because of the relatively low theoretical specific capacity of Sb (~660 mA h g^{-1}). Without the addition of CNTs, the SnSb@NCNFs control sample can still encapsulate SnSb nanodots in the NCNFs (Fig. S3c and f†), but it exhibits relatively low reversible capacity and rate capability in fresh cells and after 100 cycles at 100 mA g^{-1} (Fig. S4†), owing to the inferior conductivity. The morphology and microstructure variations of the SnSb-CNTs@NCNFs electrode after 100 cycles at 100 mA g^{-1} were also characterized (Fig. S5†), showing a layer of the homogeneously covered SEI film with a thickness of ~8 nm. Benefitting from the stable SEI film, the SnSb-CNTs@NCNFs electrode demonstrates highly reversible Li-storage performances.

The long-term cycling stability at high current densities is vital to LIBs, especially for high-power applications (*e.g.* electric vehicles and power grids). Thus, a high current density of 2000 mA g^{-1} was applied to investigate the high-rate stability of SnSb-CNTs@NCNFs, as shown in Fig. 3e. A high reversible discharge capacity of 754 mA h g^{-1} was achieved in the 10th cycle, and still remained at 522 mA h g^{-1} after 500 cycles. Notably, the discharge capacity can still reach 451 mA h g^{-1} even after 1000 cycles at 2000 mA g^{-1}. Meanwhile, without the stabilization at low current densities, the coulombic efficiency reached as high as 72.1% at the 1st cycle, and then rapidly increased to >99% after 10 cycles, and maintained at above 99.5% in the later cycles, indicating the high structural integrity of the SnSb-CNTs@NCNFs electrode and the SEI layer covered on the surface.

To better understand the origins of the capacities, CV measurements were performed at various scan rates ranging from 0.2 to 1.0 mV s^{-1} (Fig. 4a). The measured current at different scan rates obeys the power law:[41]

$$i\ (\mathrm{V}) = av^b \tag{3}$$

$$\log i\ (\mathrm{V}) = b \log v + \log a \tag{4}$$

where i, v, and a and b represent the measured current, the scan rate and the adjustable parameters, respectively. If the b-value is 0.5, the diffusion process is dominant, and if the b-value is 1.0, the electrode is controlled by the capacitive response. As presented in Fig. 4b, for the cathodic process, around the potential of 0.8 V, the b-value is close to 0.5, indicating that the capacity mainly comes from the diffusion process. At higher or lower potentials, the b-value is in the range of 0.6–0.8, suggesting that a part of the capacity originates from capacitive contribution. During the anodic process, the b-values are 0.560 and 0.573 at 0.6 V and 1.2 V, respectively, indicating the contribution of conversion reactions at low potentials; however, at higher potentials, the b-values increase to 1.0, suggesting that the capacitive response plays a more vital role with the rise of potential. More accurate capacitive and diffusion contributions can be evaluated according to the following equations:[42]

$$i\ (\mathrm{V}) = k_1 v^{1/2} + k_2 v \tag{5}$$

$$i\ (\mathrm{V})/v^{1/2} = k_1 + k_2 v^{1/2} \tag{6}$$

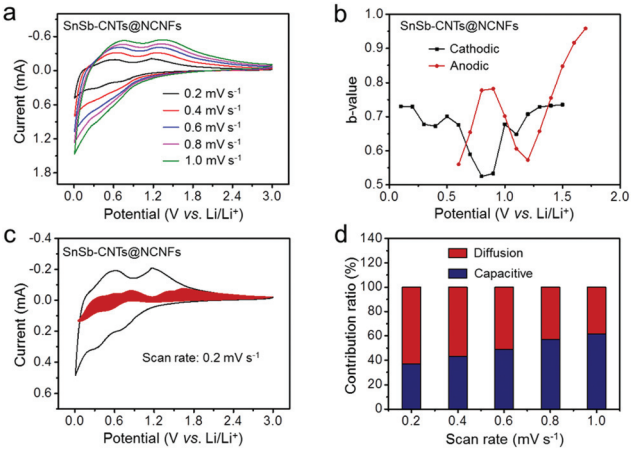

Fig. 4 Electrochemical kinetics analysis of SnSb-CNTs@NCNFs. (a) CV curves at various scan rates from 0.2 to 1.0 mV s^{-1} within 0.01–3.0 V *vs.* Li/Li^+. (b) The *b*-values as a function of applied voltage during anodic and cathodic sweeps. (c) The contributions of capacitive-controlled and diffusion-limited processes to the total current at a scan rate of 0.2 mV s^{-1} (the capacitive contribution is shown in the red region). (d) The contribution ratios of capacitive- and diffusion-controlled capacities at various scan rates.

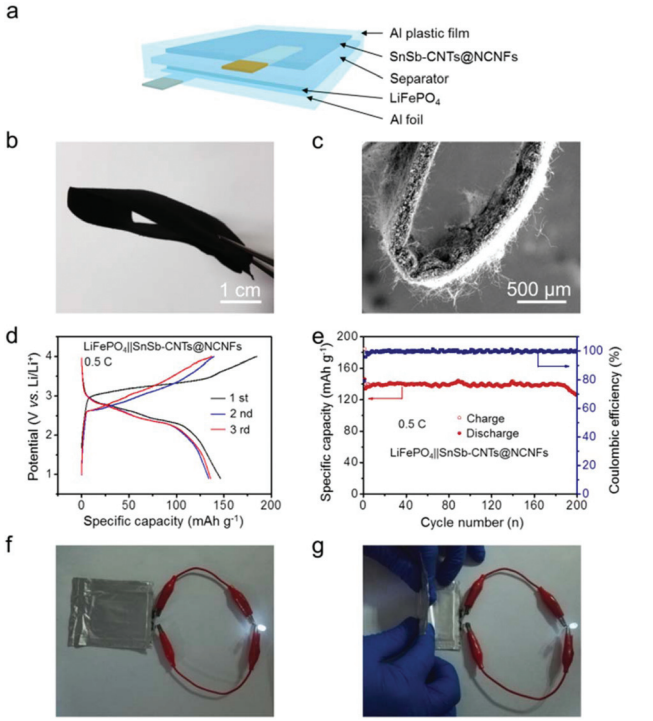

Fig. 5 (a) Schematic diagram of the soft-packed full battery assembled with the freestanding SnSb-CNTs@NCNFs anode and the $LiFePO_4$ based cathode. (b, c) Photograph and SEM images of the bent SnSb-CNTs@NCNFs electrodes. (d) Discharge–charge curves and (e) cycling performance of the as-prepared soft-packed full battery. (f, g) Photographs of the soft-packed battery based on the SnSb-CNTs@NCNFs anode lighting a LED during bending–unbending processes.

where $k_1v^{1/2}$ and k_2v refer to the diffusion and capacitive dominant processes, respectively. The value of k_1 and k_2 can be obtained from the plots of i (V)/$v^{1/2}$ *vs.* $k_2v^{1/2}$. As presented in Fig. 4c, the diffusion-controlled capacity is dominated around the peak potential, while the capacitive contribution mainly occurs at high voltage and accounts for about 36.8% to the total capacity at 0.2 mV s^{-1}. Along with the increase of the scan rate, the capacitive contribution gradually increases to 42.9%, 48.6%, 56.9%, and 61.4% at the scan rates of 0.4, 0.6, 0.8, and 1.0 mV s^{-1}, respectively (Fig. 4d). These results suggest that both the diffusion and capacitive response contribute to the high reversible capacity and play important roles in enhancing the Li-storage performances of SnSb-CNTs@NCNFs.

Encouraged by the good performances in half cells, we further evaluated the practicability of SnSb-CNTs@NCNFs in soft-packed full cells. As shown in Fig. 5a, the flexible pouch full cell was assembled with the SnSb-CNTs@NCNFs anode, glass fiber paper separator, and $LiFePO_4$ based cathode, respectively. The SnSb-CNTs@NCNFs electrodes remained structurally intact at the bending state, indicating good flexibility (Fig. 5b and c). When tested between 0.9 and 4.0 V, the flexible full cell shows a high initial discharge capacity of 147 mA h g^{-1} at 0.5 C based on the mass of $LiFePO_4$, and the output voltage is mainly above 2.0 V (Fig. 5b). The discharge capacity maintains at 126 mA h g^{-1} after 200 cycles, corresponding to a high capacity retention of 85.7% with a high coulombic efficiency of 99.5% (Fig. 5c). The charged flexible full cells are capable of lighting a light emitting diode (LED) in both flat and bent states (Fig. 5d and e), indicating the good flexibility of the SnSb-CNTs@NCNFs electrode.

Conclusions

In summary, we demonstrate the preparation of the SnSb-CNTs@NCNFs anode by confining intermetallic SnSb nanodots into CNT reinforced NCNFs as flexible anode materials for LIBs. The ultrafine SnSb nanodots provide a high electrochemical surface area, ensuring the high utility rate of the active material. The SnSb nanodots are well distributed in the NCNFs and thus avoid agglomeration during continuous cycling. The introduction of CNTs can effectively enhance the conductivity and robustness of the electrode. Moreover, the electrode is free of polymer binders, conducting additives and current collectors. Consequently, the SnSb-CNTs@NCNFs electrode exhibits outstanding electrochemical properties such as high reversible capacity, good rate capability and ultra-long cycling performance, and delivers remarkable performances in flexible full cells. We hope that this study may provide useful insights into the design of intermetallic compound-based electrode materials for advanced LIBs.

Conflicts of interest

There are no conflicts to declare.

Acknowledgements

This work was supported by the National Key R&D Program of China (2015CB659300, 2016YFB0700600, and 2017YFA0208200), the Projects of NSFC (21872069, 51761135104, and 21573108), the Natural Science Foundation of Jiangsu Province (BK20180008), the High-Level Entrepreneurial and Innovative Talents Program of Jiangsu Province, and the Fundamental Research Funds for the Central Universities of China.

Notes and references

1 B. Dunn, H. Kamath and J. M. Tarascon, *Science*, 2011, **334**, 928–935.
2 K. T. Nam, D. W. Kim, P. J. Yoo, C. Y. Chiang, N. Meethong, P. T. Hammond, Y. M. Chiang and A. M. Belcher, *Science*, 2006, **312**, 885–888.
3 L. Wang, B. Chen, J. Ma, G. Cui and L. Chen, *Chem. Soc. Rev.*, 2018, **47**, 6505–6602.
4 J. K. Choi and D. Aurbach, *Nat. Rev. Mater.*, 2016, **1**, 16013.
5 L. Mai, X. Tian, X. Xu, L. Chang and L. Xu, *Chem. Rev.*, 2014, **114**, 11828–11862.
6 A. Vlad, N. Singh, C. Galande and P. M. Ajayan, *Adv. Energy Mater.*, 2015, **5**, 1402115.
7 S. Chu, Y. Cui and N. Liu, *Nat. Mater.*, 2017, **16**, 16–22.
8 R. Schmuch, R. Wagner, G. Horpel, T. Placke and M. Winter, *Nat. Energy*, 2018, **3**, 267–278.
9 V. Zinth, C. von Luders, M. Hofmann, J. Hattendorff, I. Buchberger, S. Erhar, J. Rebelo-Kornmeier, A. Jossen and R. Gilles, *J. Power Sources*, 2014, **271**, 152–159.
10 Z. Li, J. Huang, B. Y. Liaw, V. Metzler and J. Zhang, *J. Power Sources*, 2014, **254**, 168–182.
11 X. Li, J. Yang, Y. Hu, J. Wang, Y. Li, M. Cai, R. Li and X. Sun, *J. Mater. Chem.*, 2012, **22**, 18847–18853.
12 L. Cui, L. Hu, J. W. Choi and Y. Cui, *ACS Nano*, 2010, **4**, 3671–3678.
13 Z. Yuan, H. Peng, J. Huang, X. Liu, D. Wang, X. Cheng and Q. Zhang, *Adv. Funct. Mater.*, 2014, **24**, 6105–6122.
14 S. Choi, T. Kwon, A. Coskun and J. W. Choi, *Science*, 2017, **357**, 279–283.
15 Q. Xu, J. Li, J. Sun, Y. Yin, L. Wan and Y. Guo, *Adv. Energy Mater.*, 2017, **7**, 1601481.
16 X. Wang, L. Fan, D. Gong, J. Zhu, Q. Zhang and B. Lu, *Adv. Funct. Mater.*, 2016, **26**, 1104–1111.
17 M. Mao, F. Yan, C. Cui, J. Ma, M. Zhang, T. Wang and C. Wang, *Nano Lett.*, 2017, **17**, 3830–3836.
18 J. Qin, C. He, N. Zhao, Z. Wang, C. Shi, E. Liu and J. Li, *ACS Nano*, 2014, **8**, 1728–1738.
19 J. Sun, G. Zheng, H. Lee, N. Liu, H. Wang, H. Yao, W. Yang and Y. Cui, *Nano Lett.*, 2014, **14**, 4573–4580.
20 W. Li, Z. Yang, M. Li, Y. Jiang, X. Wei, X. Zhong, L. Gu and Y. Yu, *Nano Lett.*, 2016, **16**, 1546–1553.
21 J. Liu, L. Yu, C. Wu, Y. Wen, K. Yin, F. Chiang, R. Hu, J. Liu, L. Sun and L. Gu, *Nano Lett.*, 2017, **17**, 2034–2042.
22 N. Wang, Z. Bai, Y. Qian and J. Yang, *Adv. Mater.*, 2016, **28**, 4126–4133.
23 F. Yang, F. Yu, Z. Zhang, K. Zhang, Y. Lai and J. Li, *Chem. – Eur. J.*, 2016, **22**, 2333–2338.
24 H. Zhang, X. Huang, O. Noonan, L. Zhou and C. Yu, *Adv. Funct. Mater.*, 2017, **27**, 1606023.
25 W. Luo, F. Li, J. Gaumet, P. Magri, S. Diliberto, L. Zhou and L. Mai, *Adv. Energy Mater.*, 2018, **8**, 1703237.
26 Y. Zou and Y. Wang, *ACS Nano*, 2011, **5**, 8108–8114.
27 L. Baggetto, P. Ganesh, C. Sun, R. A. Meisner, T. A. Zawodzinski and G. M. Veith, *J. Mater. Chem. A*, 2013, **1**, 7985–7994.
28 L. Fan, J. Zhang, Y. Zhu, X. Zhu, J. Liang, L. Wang and Y. Qian, *RSC Adv.*, 2014, **4**, 62301–62307.
29 X. Niu, H. Zhou, Z. Li, X. Shan and X. Xia, *J. Alloys Compd.*, 2015, **620**, 308–314.
30 X. Xia, Z. Li, H. Zhou, Y. Qiu and C. Zhang, *Electrochim. Acta*, 2016, **222**, 765–772.
31 J. Li, J. Pu, Z. Liu, J. Wang, W. Wu, H. Zhang and H. Ma, *ACS Appl. Mater. Interfaces*, 2017, **9**, 25250–25256.
32 A. Birrozzi, F. Maroni, R. Raccichini, R. Tossici, R. Marassi and F. Nobili, *J. Power Sources*, 2015, **294**, 248–253.
33 J. Leibowitz, E. Allcorn and A. Manthiram, *J. Power Sources*, 2015, **279**, 549–554.
34 K. Shiva, H. B. Rajendra and A. J. Bhattacharyya, *ChemPlusChem*, 2015, **80**, 516–521.
35 X. Tang, F. Yan, Y. Wei, M. Zhang, T. Wang and T. Zhang, *ACS Appl. Mater. Interfaces*, 2015, **7**, 21890–21897.
36 S. Fan, T. Sun, X. Rui, Q. Yan and H. H. Hug, *J. Power Sources*, 2012, **201**, 288–293.
37 J. Seo and C. Park, *J. Mater. Chem. A*, 2013, **1**, 15316–15322.
38 C. Park and H. Sohn, *Electrochim. Acta*, 2009, **54**, 6367–6373.
39 K. Liang, K. Marcus, S. Zhang, L. Zhou, Y. Li, S. T. De Oliveira, N. Orlovskaya, Y. Sohn and Y. Yang, *Adv. Energy Mater.*, 2017, **7**, 1701309.
40 K. Liang, L. Ju, S. Koul, A. Kushima and Y. Yang, *Adv. Energy Mater.*, 2019, **9**, 1802543.
41 K. Cao, L. Jiao, Y. Liu, H. Liu, Y. Wang and H. Yuan, *Adv. Funct. Mater.*, 2015, **25**, 1082–1089.
42 V. Augustyn, J. Come, M. A. Lowe, J. W. Kim, P. L. Taberna, S. H. Tolbert, H. D. Abruna, P. Simon and B. Dunn, *Nat. Mater.*, 2013, **12**, 518–522.

